

Article

# Characterization of Microstructural Evolution for a Near- $\alpha$ Titanium Alloy with Different Initial Lamellar Microstructures

Hui Li \*, Zhanglong Zhao \*, Yongquan Ning, Hongzhen Guo and Zekun Yao

School of Materials Science and Engineering, Northwestern Polytechnical University, Xi'an 710072, China; luckyning@nwpu.edu.cn (Y.N.); hzguo@nwpu.edu.cn (H.G.); yzekun@nwpu.edu.cn (Z.Y.)

\* Correspondence: lhjy926@163.com (H.L.); zlzha@nwpu.edu.cn (Z.Z.); Tel.: +86-29-88493744 (H.L. &amp; Z.Z.)

Received: 18 November 2018; Accepted: 8 December 2018; Published: 10 December 2018



**Abstract:** The effects of initial lamellar thickness on microstructural evolution and deformation behaviors of a near- $\alpha$  Ti-5.4Al-3.7Sn-3.3Zr-0.5Mo-0.4Si alloy were investigated during isothermal compression in  $\alpha + \beta$  phase field. Special attention was paid to microstructural conversion mechanisms for  $\alpha$  lamellae with different initial thicknesses. The deformation behaviors, including flow stress, temperature sensitivity, and strain rate sensitivity, and processing maps and their dependence on initial lamellar thickness were discussed. The detailed microstructural characterizations in different domains of the developed processing maps were analyzed. The results showed that the peak efficiency of power dissipation decreased with increasing initial lamellar thickness. The interaction effects with different extents of globularization, elongating, kinking, and phase transformation of lamellar  $\alpha$  accounted for the variation in power dissipation. The flow instability region appeared to expand more widely for thicker initial lamellar microstructures during high strain rate deformation due to flow localization and local lamellae kinking. The electron backscatter diffraction (EBSD) analyses revealed that the collaborative mechanism of continuous dynamic recrystallization (CDRX) and discontinuous dynamic recrystallization (DDRX) promoted the rapid globularization behavior for the thinnest acicular initial microstructure, whereas in case of the initial thick lamellar microstructure, CDRX leading to the fragmentation of lamellae was the dominant mechanism throughout the deformation process.

**Keywords:** near- $\alpha$  titanium alloy; alpha lamellar thickness; processing map; microstructure evolution; deformation mechanism

## 1. Introduction

Near- $\alpha$  titanium alloy with an attractive combination of properties has been extensively applied as advanced structural material for aeroengine components [1,2]. The Ti-5.4Al-3.7Sn-3.3Zr-0.5Mo-0.4Si alloy discussed in the present work is a type of near- $\alpha$  high-temperature titanium alloy for advanced gas turbine compressor disk application, which exhibits excellent thermal capability properties under the servicing temperature of 600 °C [3,4]. In general, the mechanical properties linked with the final microstructures of titanium alloys are dependent on a set of typical hot-working steps involving primary cogging in  $\beta$  phase field, thermo-mechanical processes below the  $\beta$ -transus, and subsequent heat treatment [5]. Therefore, it is necessary to have an in-depth knowledge about the deformation behavior, hot workability, and microstructure development of the material in the process in order to obtain optimum process schedules and achieve the desired microstructure and mechanical properties.

Over the years, hot deformation behaviors of titanium alloys with various initial microstructures have received considerable attention due to their significant influence. For example, Jackson et al. [6]

analyzed the flow softening behavior of a near- $\beta$  Ti-10V-2Fe-3Al alloy with two initial microstructures and revealed that the alloy with Widmanstätten  $\alpha$  platelets displayed more flow softening than that with globular  $\alpha$ . Lin et al. [7] discussed the hot tensile properties for a Ti-6Al-4V alloy with different initial microstructures including basket-weave, globular-lamellar, and equiaxed microstructures. Gao et al. [8] studied the effect of initial nonuniform microstructure on flow behavior and microstructure evolution of a near- $\alpha$  TA15 alloy. During the cooling from  $\beta$  phase field, lamellar  $\alpha$  with diverse morphologies were formed. Semiatin and the coauthors systematically investigated the dependence of the flow softening mechanism on various initial microstructures, including initial lamellar  $\alpha$  thickness [9], colony size [10], morphology of lamellar  $\alpha$  [11], and texture [12]. These works have a detailed description for understanding the deformation behavior and microstructural features of titanium alloys. However, most of the works were mainly focused on the effect of initial microstructures on globularization kinetics and flow softening behavior. Moreover, the number of studies related to the correlation among initial lamellar thickness, processing maps, and microstructure evolution for near- $\alpha$  titanium alloy is insufficient. In particular, little attention has been paid to discovering various evolution mechanisms for the lamellar microstructure with different initial thicknesses.

Therefore, the objective of the present paper is to characterize the evolution behavior of lamellar  $\alpha$  with different initial thicknesses for the Ti-5.4Al-3.7Sn-3.3Zr-0.5Mo-0.4Si alloy. To this end, the effects of initial lamellar thickness and deformation parameters on the flow behavior and processing maps were detected and analyzed. Meanwhile, microstructure evolutions of different initial lamellar microstructures for a few particular domains with varying power dissipation values in processing maps were discussed. Moreover, an interesting point of this work involved evaluating the distinct deformation mechanisms of lamellar  $\alpha$  with different initial thicknesses. The results could provide significant technical guidance for controlling the final microstructure and contribute to the development of applications in the practical production processes for the Ti-5.4Al-3.7Sn-3.3Zr-0.5Mo-0.4Si alloy.

## 2. Materials and Methods

The  $\beta$ -transus temperature of the Ti-5.4Al-3.7Sn-3.3Zr-0.5Mo-0.4Si alloy was measured at approximately 1045 °C via metallographic method. The samples for the alloy with three different initial lamellar microstructures in the present work (as shown in Figure 1) were prepared by heating to 1070 °C for 10 min, followed by various cooling rates to room temperature. Microstructure A (Figure 1a) is a typical fine acicular martensitic microstructure with an approximately 1  $\mu\text{m}$ -thick alpha platelet. The colony microstructures with average alpha lamellar thicknesses of 6  $\mu\text{m}$  and 10  $\mu\text{m}$  are referred to as microstructure B (Figure 1b) and microstructure C (Figure 1c), respectively. To investigate the deformation behavior of the alloy in  $\alpha + \beta$  phase field, cylindrical specimens of 8 mm diameter and 12 mm height were machined for isothermal compression tests which were performed on a Gleebe-3500 thermo-mechanical simulator (Data Sciences International, Inc., St. Paul, MN, USA) at deformation temperatures of 900 °C, 930 °C, 960 °C, 990 °C, and 1020 °C, with a strain rate range of 0.001–10  $\text{s}^{-1}$ . During the tests, the heating rate was 5 °C/s and soaking for 5 min to eliminate thermal gradient. After being compressed to a height reduction of 50% under a certain strain rate, the specimen was rapidly cooled down to room temperature. Then the axial sections of deformed specimens were prepared for microstructure examination. The surfaces of compressed specimens were mechanically polished and then chemically etched in a solution of 3% HF, 6% HNO<sub>3</sub> and 91% H<sub>2</sub>O, subsequently observed on an OLYMPUS-GX71 optical microscope (Olympus Corporation, Tokyo, Japan) to obtain the metallographic microstructures. Electron backscatter diffraction (EBSD) samples were electro-polished in the solution of 5% perchloric acid and 95% methanol for about 30 s at approximately 25 °C with a voltage of 30 V. A TESCAN MIRA3 XMU scanning electron microscope equipped with a Nordlys Max EBSD detector (TESCAN, Brno, Czech Republic) was used for EBSD measurement.

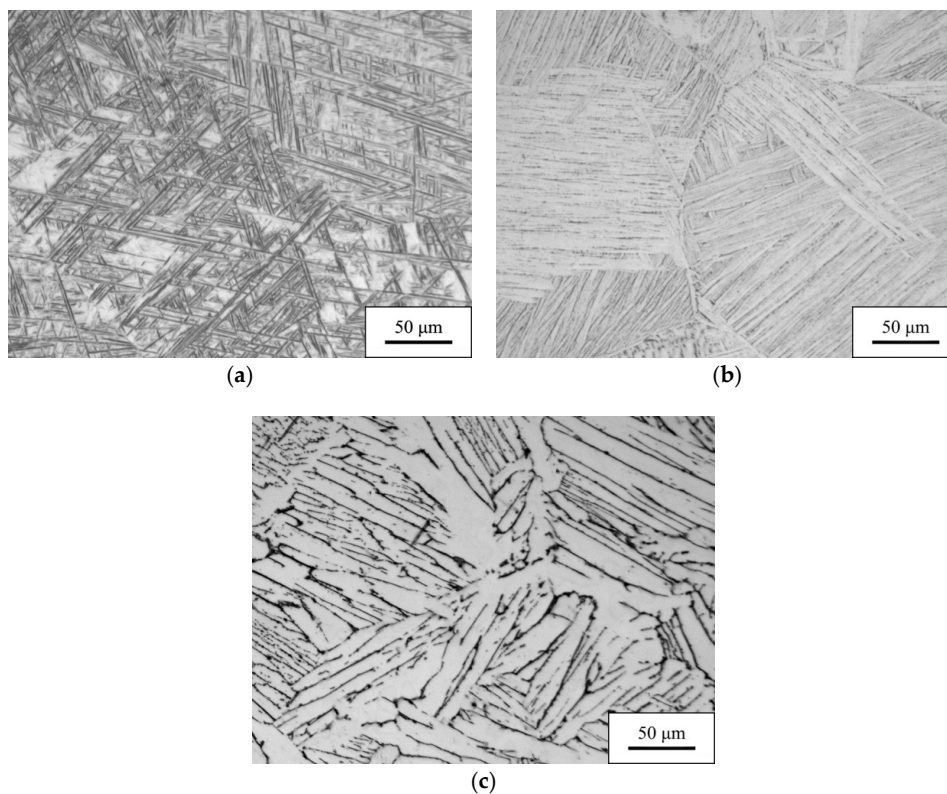


**Figure 1.** Initial microstructure of the Ti-5.4Al-3.7Sn-3.3Zr-0.5Mo-0.4Si alloy before deformation with different lamellar thicknesses: (a) microstructure A; (b) microstructure B; (c) microstructure C.

### 3. Results and Discussion

#### 3.1. Flow Behavior

The effects of initial lamellar microstructures and deformation parameters on the flow stress of the Ti-5.4Al-3.7Sn-3.3Zr-0.5Mo-0.4Si alloy are shown in Figure 2. The flow stress was significantly dependent on initial lamellar thickness and deformation parameters. The similar variation trend with a quick increasing to peak stress and a noticeable flow softening were observed in the exhibited stress-strain curves. When deformed to a large strain under some conditions, the flow stress curves may reach a steady state. Under given deformation conditions, the studied alloy with initial microstructure A (initial lamellar thickness: 1  $\mu\text{m}$ ) showed obviously higher flow stress and flow softening behavior than that with microstructures B (6  $\mu\text{m}$ ) and C (10  $\mu\text{m}$ ). It was observed that the increasing lamellar thickness of  $\alpha$  phase could result in the decrease in deformation resistance.

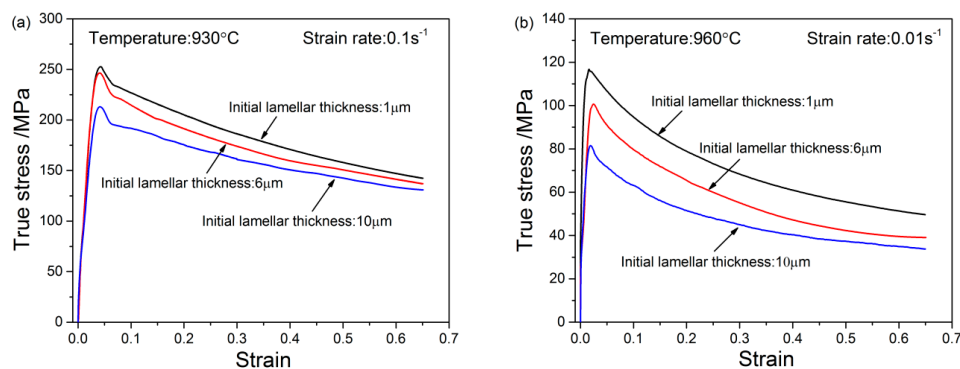


**Figure 2.** Typical flow stress–strain curves of the Ti-5.4Al-3.7Sn-3.3Zr-0.5Mo-0.4Si alloy with different initial lamellar microstructures.

The steady state flow stress (stress at strain of 0.65 in the present work) changing with deformation temperatures for the alloy with three initial lamellar microstructures is shown in Figure 3a. It can be seen that the flow stress decreases rapidly with deformation temperature increasing from 900 °C to 960 °C, especially at a high strain rate, whereas the flow stress becomes less sensitive to temperature above the temperature of 990 °C. The work by Wanjara et al. [13] suggested that the transition trend in flow stress may take place at a temperature between about 70 °C and 40 °C below the  $\beta$ -transus temperature of the material, which concurs with the present result. The temperature sensitivity can be evaluated by a parameter  $S$ , defined as the following equation [2]:

$$S = \frac{1}{T} \frac{\partial \log \sigma}{\partial (1/T)}. \quad (1)$$

Based on experimental results, the temperature sensitivity parameters of the alloy with different initial lamellar microstructures and strain rates at a given true strain of 0.65 were obtained using Equation (1) and shown in Figure 3. The temperature sensitivity curves obtained exhibit almost a similar trend with the deformation temperature. Regardless of strain rate and initial microstructure, the sensitivity parameter displays a peak value at the temperature of 960 °C, which indicates that a fine grain structure of the alloy may be exhibited in this temperature range [2]. The values of the temperature sensitivity parameter are very small and less than 2 at a lower temperature (900 °C) and higher strain rates ( $1 \text{ s}^{-1}$ ,  $10 \text{ s}^{-1}$ ), which implies that the alloy may exhibit instable flow under these conditions.

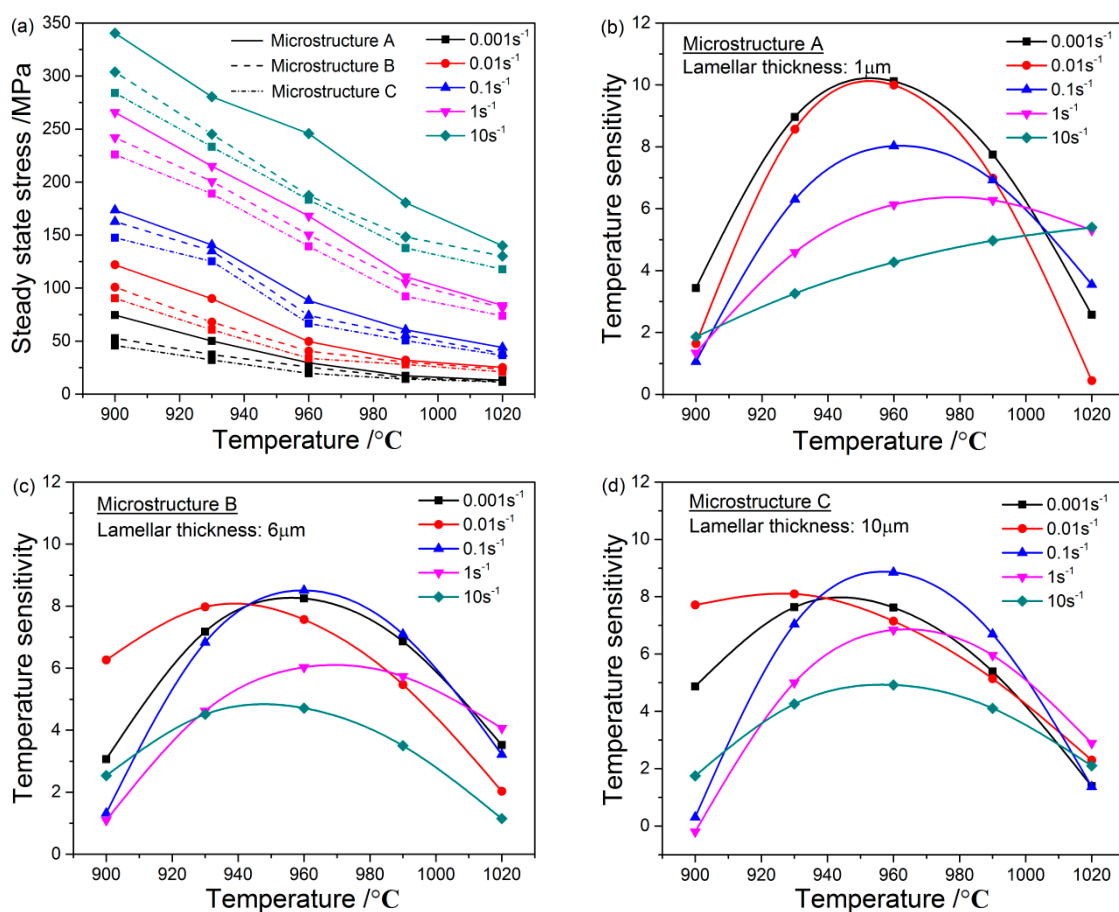


**Figure 3.** Variation of (a) steady state flow stress and temperature sensitivity parameter for the Ti-5.4Al-3.7Sn-3.3Zr-0.5Mo-0.4Si alloy with different initial lamellar microstructures: (b) microstructure A; (c) microstructure B; (d) microstructure C.

The effects of deformation parameters and initial lamellar thicknesses on strain rate sensitivity ( $m = \partial \ln \sigma / \partial \ln \dot{\epsilon}$ ) for the alloy deformed at strain of 0.65 are shown in Figure 4. The variations in strain rate sensitivity, along with the change in processing parameters, are closely associated with the microstructure evolution. Figure 4 indicates that strain rate sensitivity for the studied alloy with different initial microstructures increases with the decrease in the strain rate, showing results which are similar to the results obtained from other titanium alloys [14–16]. The values of strain rate sensitivity for the present alloy are in the range of 0.1 to 0.4, and the higher values are obtained at lower strain rates for almost all temperatures except at 1020 °C. At lower strain rates of 0.001 s<sup>-1</sup> and 0.01 s<sup>-1</sup>, the  $m$  value increases to the maximum and then decreases with the rising temperature. When the alloy is deformed at a higher strain rate, the value of  $m$  presents a roughly increasing tendency with the rising temperature. The maximum strain rate sensitivity of 0.40, 0.36, and 0.32 was found to exist at a strain rate of 0.001 s<sup>-1</sup> and a deformation temperature of 960 °C for the alloy with initial microstructure A, B, and C, respectively. The results show that the strain rate sensitivity values increase with the decrease in the initial lamellar thickness. Such increments may be associated with the occurrence of grain-boundary sliding and different dynamic globularization kinetics which increase as the alpha lamellar thickness decreases [10,17].

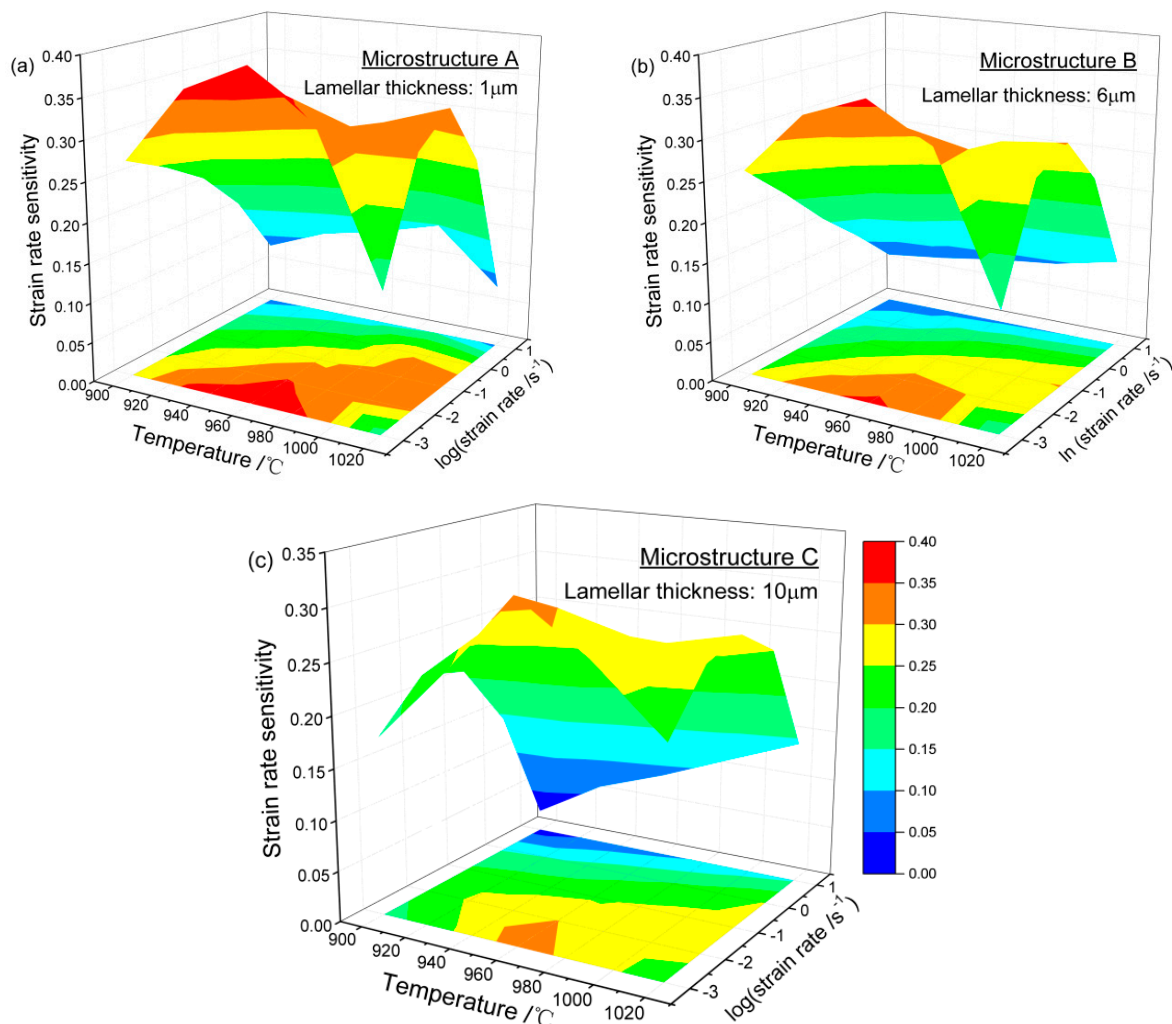


**Figure 4.** Strain rate sensitivity exponent of the Ti-5.4Al-3.7Sn-3.3Zr-0.5Mo-0.4Si alloy with initial microstructures of: (a) microstructure A; (b) microstructure B; (c) microstructure C.

### 3.2. Effect of Initial Lamellar Thickness on Processing Maps

The approach using processing maps is an effective method to analyze hot deformation behavior, optimize processing parameters and control microstructures of the materials. During the hot-working process, based on the dynamic material modeling, the efficiency of power dissipation ( $\eta$ ) is used to evaluate the power dissipation capacity of the material and is expressed as follows [18]:

$$\eta = 2m/(m + 1), \quad (2)$$

where  $m$  is the strain rate sensitivity. The occurrence of flow instability is defined as follows [19]:

$$\xi(\dot{\epsilon}) = \frac{\partial \ln[m/m + 1]}{\partial \ln \dot{\epsilon}} + m < 0. \quad (3)$$

The processing maps of the Ti-5.4Al-3.7Sn-3.3Zr-0.5Mo-0.4Si alloy with three different initial lamellar microstructures for the true strain of 0.65 are shown in Figure 5, in which iso-contour numbers represent the  $\eta$  values and shaded regions represent the instable domains. It is obvious that the initial lamellar thickness and processing parameters have a noticeable impact on the efficiency of power dissipation for the studied alloy. The  $\eta$  value had a similar variation trend with strain rate sensitivity which decreased with the increasing strain rate and the decreasing deformation temperature under lower strain rates. As shown in Figure 5a, the peak efficiency domain distributed over at the temperature range of 940 °C to 970 °C and strain rate of 0.001 s<sup>-1</sup> to 0.003 s<sup>-1</sup> under the present experimental conditions with a distinct maximum value of 0.57 occurring at 960 °C/0.001 s<sup>-1</sup>. The alloy with initial microstructure A also exhibited high temperature sensitivity (Figure 3) and strain rate sensitivity exponent (Figure 4) under the same processing conditions. When the alloy was deformed in relatively higher strain rate regions (above 1.5 s<sup>-1</sup>), the  $\xi$  values were negative and flow instability occurred. For the alloy with microstructure B, the variation in the  $\eta$  value was similar and the safe region was located in the range of 900–1020 °C when the strain rate was less than 1 s<sup>-1</sup>, as is shown in Figure 5b. The  $\eta$  value in the stable region was greater than 0.30, in which an area with a peak efficiency of approximately 0.53 existed. The flow instability region appeared to expand more widely than that for the alloy with microstructure A. For the alloy with microstructure C, the peak efficiency region occurred at 940–980 °C/0.001–0.01 s<sup>-1</sup> with a maximum value of 0.48 which was lower than that of initial microstructures A and B. The flow instability extended to a lower strain rate domain when the alloy was deformed at the low temperature of 900 °C.

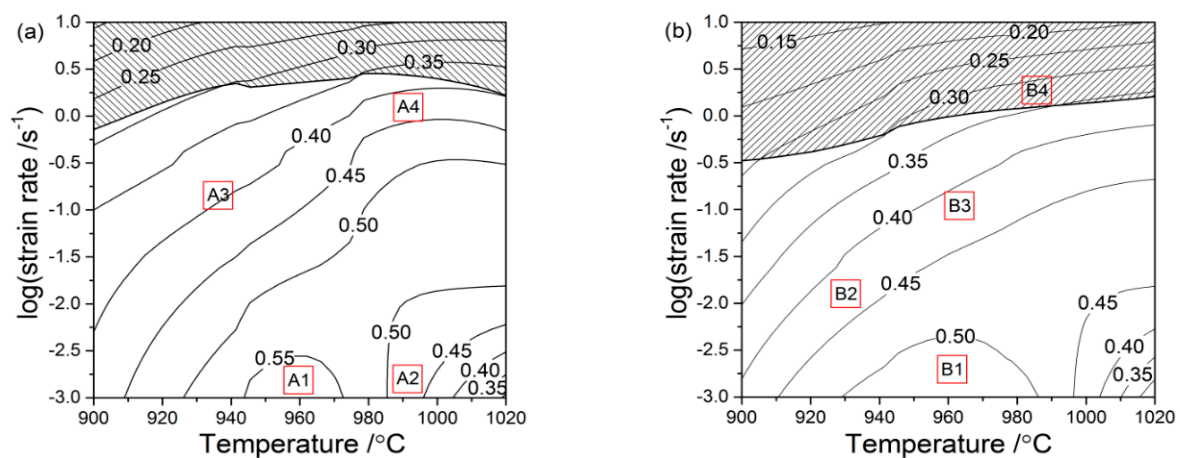
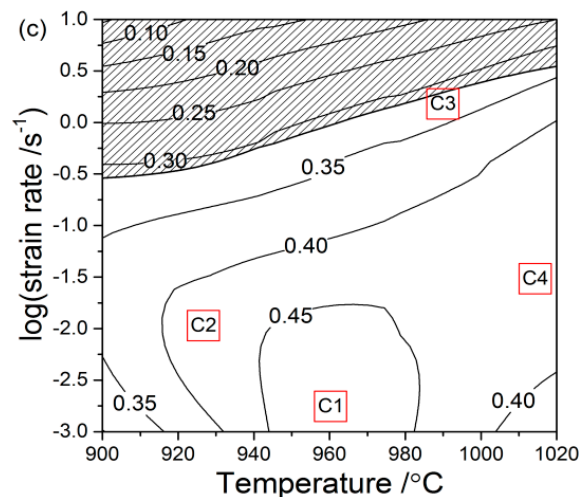


Figure 5. Cont.



**Figure 5.** Processing maps of the Ti-5.4Al-3.7Sn-3.3Zr-0.5Mo-0.4Si alloy with different initial lamellar microstructures at strain of 0.65: (a) microstructure A; (b) microstructure B; (c) microstructure C. The iso-contour numbers represent the efficiency of power dissipation ( $\eta$ ) and the shaded regions correspond to the instable domains ( $\xi < 0$ ).

The developed processing maps revealed that the regions with high  $\eta$  value were almost positioned under deformation conditions of moderate-temperature and low-strain-rate. In addition, the peak efficiency values for the three initial lamellar microstructures all occurred at the deformation temperature of 960 °C and strain rate of 0.001 s<sup>-1</sup>. The maximum value and the regions with  $\eta$  value higher than 0.5 ( $\eta > 0.5$ ) decreased with the increase in the initial lamellar thickness, while the flow instability domain became obviously wider. The previous works indicated that the deformation mechanism of dynamic recrystallization [20] or superplasticity [21] could be responsible for the high  $\eta$  values in processing maps. Semiatin [22] suggested that the superplasticity generally appeared in the Ti-alloys with initial fine and two-phase equiaxed microstructure features. For the present work, the studied alloy with initial lamellar microstructure having large grains did not satisfy the microstructural requirement for obtaining superplasticity [14]. Therefore, the peak power dissipation efficiency might be associated with dynamic recrystallization. The differences among the three processing maps may be due to the multiple microstructural evolution of the Ti-5.4Al-3.7Sn-3.3Zr-0.5Mo-0.4Si alloy with three initial lamellar thicknesses during the deformation at elevated temperature. To clarify the underlying deformation mechanisms, the characterization of deformation behaviors for different domains in processing maps was investigated according to microstructure observations and discussions.

### 3.3. Microstructural Analysis

In order to investigate deformation behavior and microstructure evolution, the microstructures of a few domains with varying efficiency of power dissipation values in processing maps for the present alloy with three initial lamellar microstructures were characterized and analyzed, as illustrated in Figures 6–8. The selected domains in the processing map with strain of 0.65 for the alloy with initial microstructure A are marked with different numbers as follows: A1, 960 °C and 0.001 s<sup>-1</sup>; A2, 990 °C and 0.001 s<sup>-1</sup>; A3, 930 °C and 0.1 s<sup>-1</sup>; and A4, 990 °C and 1 s<sup>-1</sup>. The corresponding microstructures in these domains are shown in Figure 6. Under deformation conditions of 960 °C/0.001 s<sup>-1</sup>, almost all of the initial lamellar  $\alpha$  phase was globularized and the final equiaxed  $\alpha$  phase was well distributed as seen in Figure 6a, which corresponds to the peak  $\eta$  value in the processing map. The volume fraction of  $\alpha$  phase changed slightly at deformation temperatures between 900 °C and 960 °C, but sharply decreased with the temperature increasing from 960 °C to 990 °C, as the significant phase transformation of  $\alpha$  to  $\beta$  was enhanced at a low strain rate. Compared with higher strain rates,

the globularization of  $\alpha$  lamellae was more sufficient at strain rate of  $0.001 \text{ s}^{-1}$ . With the strain rate increasing to  $0.1 \text{ s}^{-1}$ , it was evident that the morphology of  $\alpha$  phase changed in an obvious manner, which was more likely to be elongated rather than spheroidized (marked with a black arrow in Figure 6d). Thus, the  $\eta$  value at the lower strain rate was higher than that of the higher strain rate in the temperature range of  $900$  to  $990 \text{ }^\circ\text{C}$ . The deformation characteristic of flow instability regions is always attributed to adiabatic shear deformation, internal cracks, and grain boundary cavities during the hot deformation of titanium alloys [23–26]. The results in our previous work by Zhao et al. [4] showed that microstructures of the present alloy with acicular microstructure deformed in flow instability regions at a strain rate of  $10 \text{ s}^{-1}$  and exhibited flow localization bands.

The selected domains in the processing map for the alloy with initial microstructure B are marked as follows: B1,  $960 \text{ }^\circ\text{C}$  and  $0.001 \text{ s}^{-1}$ ; B2,  $990 \text{ }^\circ\text{C}$  and  $0.001 \text{ s}^{-1}$ ; B3,  $930 \text{ }^\circ\text{C}$  and  $0.01 \text{ s}^{-1}$ ; and B4,  $990 \text{ }^\circ\text{C}$  and  $1 \text{ s}^{-1}$ . The corresponding microstructures in these domains are shown in Figure 7. At the peak efficiency regions with a temperature of  $960 \text{ }^\circ\text{C}$  and a strain rate of  $0.001 \text{ s}^{-1}$ , the deformed microstructure consisted of equiaxed  $\alpha$  phase and a small amount of short lamellar  $\alpha$ , as is shown in Figure 7a. The temperature affected the microstructure in a similar way for the alloy with initial microstructure A, which only changed the volume fraction of  $\alpha$  phase but not the morphology in an obvious manner. After the alloy was deformed at the relatively higher temperature of  $990 \text{ }^\circ\text{C}/0.001 \text{ s}^{-1}$ , the volume fraction of  $\alpha$  phase further decreased and more  $\beta$ -transus microstructures were observed. The breaking up of the lamellae and  $\alpha$  phase with equiaxed morphology was generated to a greater degree at the lower strain rate. At strain rates higher than  $1 \text{ s}^{-1}$ , the microstructures exhibited extensive kinking of lamellae which formed in the colonies inclined up to  $45^\circ$  to the compression axis, as is shown in Figure 7d.

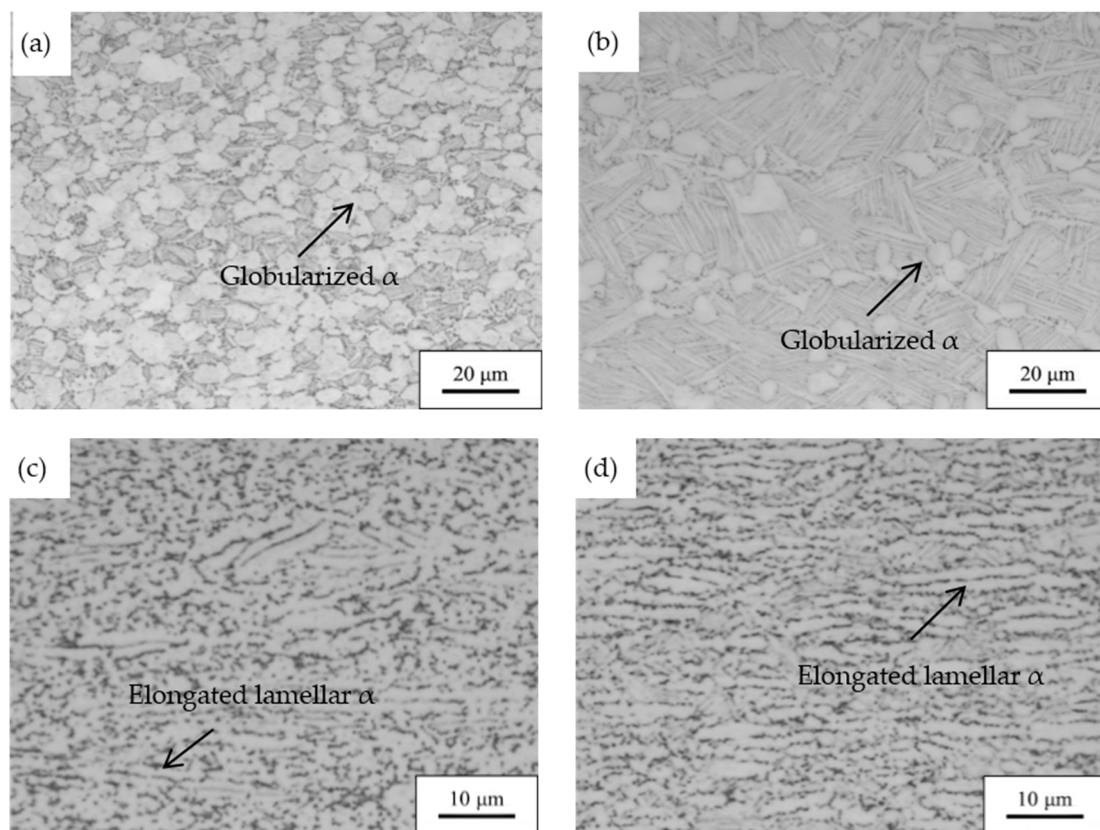


**Figure 6.** Microstructures of the Ti-5.4Al-3.7Sn-3.3Zr-0.5Mo-0.4Si alloy with initial microstructure A deformed at: (a)  $960 \text{ }^\circ\text{C}$ ,  $0.001 \text{ s}^{-1}$ ; (b)  $990 \text{ }^\circ\text{C}$ ,  $0.001 \text{ s}^{-1}$ ; (c)  $930 \text{ }^\circ\text{C}$ ,  $0.1 \text{ s}^{-1}$ ; (d)  $990 \text{ }^\circ\text{C}$ ,  $1 \text{ s}^{-1}$ .

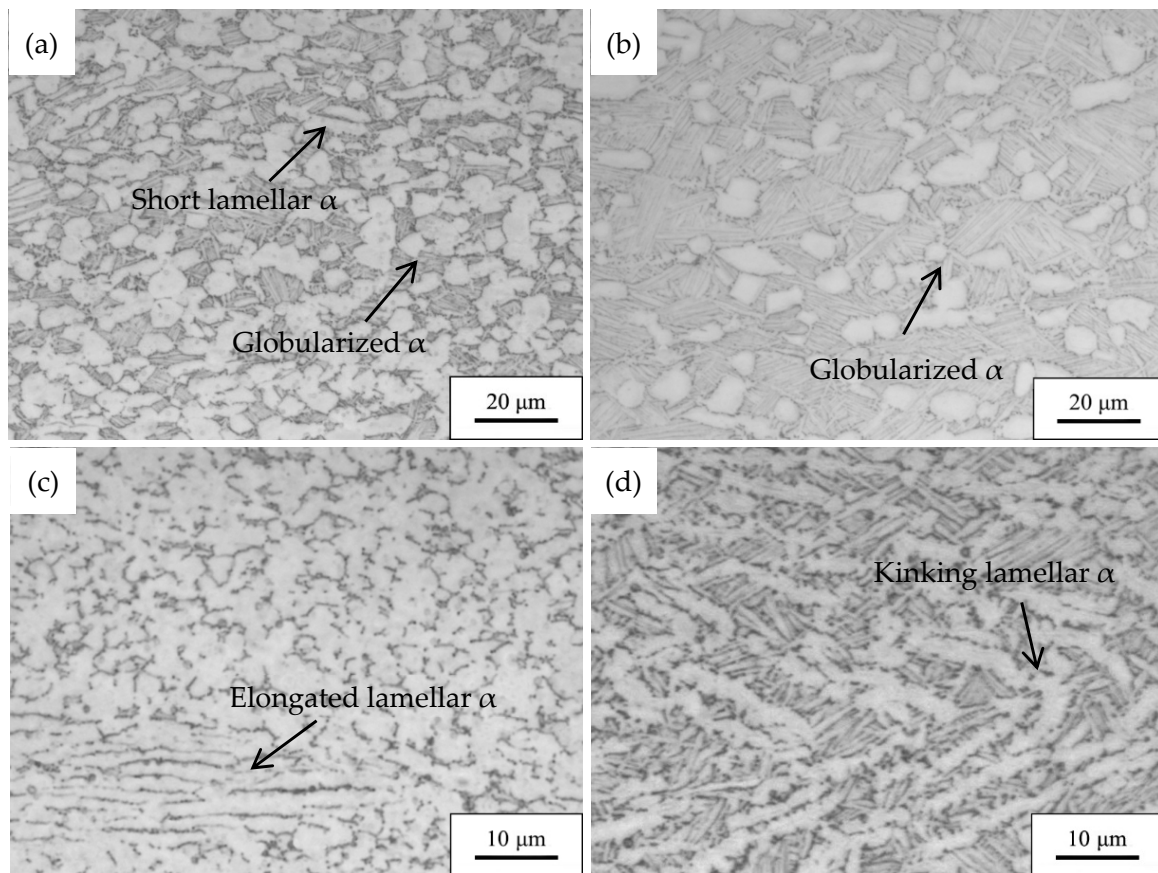


**Figure 7.** Microstructures of the Ti-5.4Al-3.7Sn-3.3Zr-0.5Mo-0.4Si alloy with initial microstructure B deformed at: (a) 960 °C, 0.001 s<sup>-1</sup>; (b) 990 °C, 0.001 s<sup>-1</sup>; (c) 930 °C, 0.01 s<sup>-1</sup>; (d) 990 °C, 1 s<sup>-1</sup>.

The selected domains in the processing map for the alloy with initial microstructure C are marked as follows: C1, at 960 °C and 0.001 s<sup>-1</sup>; C2, at 930 °C and 0.01 s<sup>-1</sup>; C3, at 990 °C and 1 s<sup>-1</sup>; and C4, at 1020 °C and 0.01 s<sup>-1</sup>. The corresponding microstructures in these domains are shown in Figure 8. At the peak efficiency dissipation region C1, the lamellae displayed an obvious trend to twirl toward the perpendicular direction to compression axis. As is labeled in Figure 8a, only a few occurrences of fragmentation of lamellae and spheroidization of  $\alpha$  phase existed because the 50% reduction of the height was insufficient for complete globularization of the alloy with initial thick lamellar microstructure. With the strain rate increasing and the temperature decreasing, the fragmentations of lamellar  $\alpha$  were restrained and more elongated ones were observed. When the alloy was deformed at near  $\beta$ -transus temperature of 1020 °C, the microstructure were similar to a  $\beta$  transformed one and the  $\beta$  grain boundaries became serrated. In addition, some dynamic recrystallization grains were formed along the elongated grain boundaries. The efficiency of power dissipation decreased at the temperature of 1020 °C in virtue of the slight increase in the  $\beta$  grain size with the decrease in the strain rate.

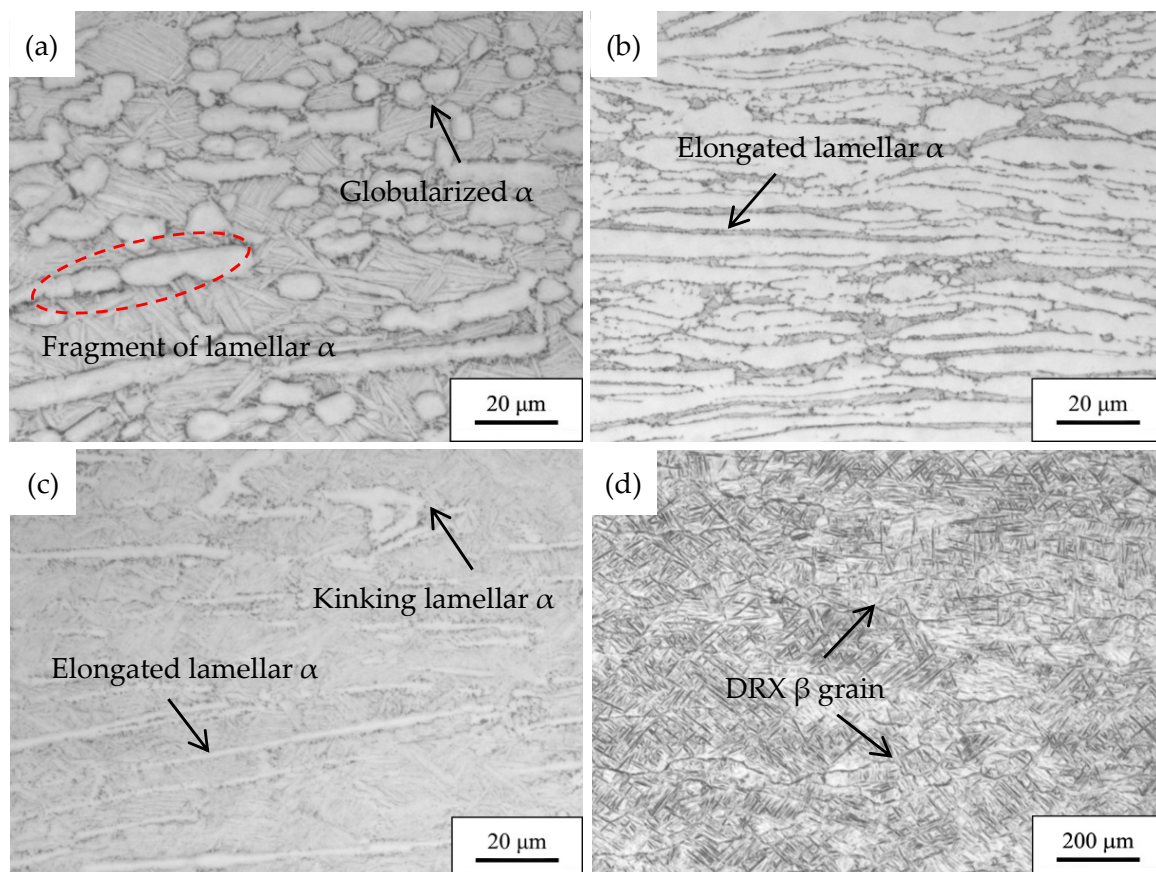


**Figure 8.** Microstructures of the Ti-5.4Al-3.7Sn-3.3Zr-0.5Mo-0.4Si alloy with initial microstructure C deformed at: (a) 960 °C, 0.001 s<sup>-1</sup>; (b) 930 °C, 0.01 s<sup>-1</sup>; (c) 990 °C, 1 s<sup>-1</sup>; (d) 1020 °C, 0.01 s<sup>-1</sup>.

### 3.4. Deformation Mechanism of Lamellar Alpha

The EBSD microstructures of the alloy with initial thin acicular lamellar alpha (microstructure A) at two regions in the specimen deformed at a temperature of 960 °C and a strain rate of 0.01 s<sup>-1</sup> are depicted in Figure 9. As a result of different local effective strains for the two regions in the deformed specimen, the microstructures displayed various characterizations. As is seen in Figure 9a, there were a certain number of residual lamellar α in region A, which was attributed to the insufficient and non-uniform deformation. In addition, some new fine grains with equiaxed morphology can be observed around the lamellar α. The volume fraction of globular α grains was greatly affected by the applied strain and it increased from 65.1% (region A) to 80.8% (region B) with the strain increasing. Moreover, the colors in the inverse pole figure (IPF) maps also change noticeably and the distribution becomes more uniform in Figure 9b. The strain had a significant influence on the frequency of the low-angle grain boundaries (LABs, misorientation between 2° and 15°) and high-angle grain boundaries (HABs, misorientation over 15°). The greater strain resulted in the number of LABs decreasing and of HABs increasing, which can be related to the microstructure conversion from lamellae to equiaxed.

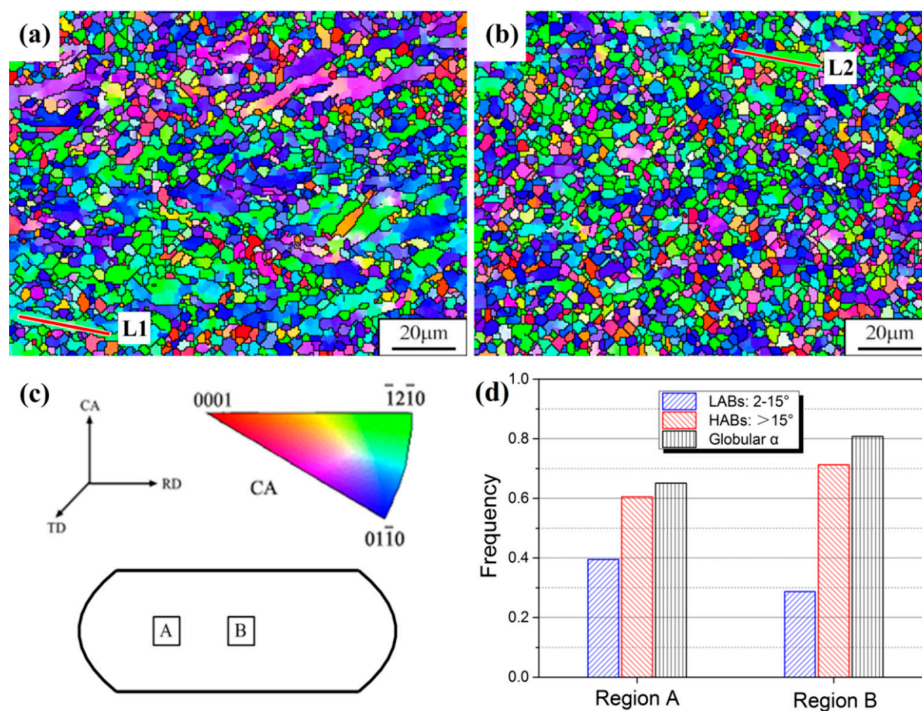


**Figure 9.** Electron backscatter diffraction (EBSD) inverse pole figure (IPF) maps of the alloy with initial microstructure A deformed at  $960\text{ }^{\circ}\text{C}/0.01\text{ s}^{-1}$ : (a) region A; (b) region B; (c) schematic of the microstructure observation locations; (d) relative frequency of misorientation.

Figure 10 shows the variation in orientation accumulations which are detected along the white line marked in Figure 9. It is noted that orientations along the lamellar  $\alpha$  change broadly and the cumulative misorientation of line L1 is lower than  $10^{\circ}$ , whereas the maximum value for L2 exceeds  $30^{\circ}$ . According to the point to origin profile, the two lines can be described as continuous accumulation for L1 and discontinuous multi-peak orientation distribution for L2, respectively. The small misorientation angle in point to point line for the continuous accumulation profile in L1 is observed, and it indicates a long-range continuous lattice distortion which can be associated with the formation of subgrains [27,28]. The point to point line of L2 displays alternating lattice orientation with an order of  $1\text{--}10^{\circ}$  between the neighboring points leading to the multi-peaks. This may be attributed to the gradual increasing of the low misorientation angle to a higher value in the lamellar  $\alpha$  with the strain increasing. These two representative types of orientation accumulations profiles are also observed in other deformed microstructures. The heterogeneous evolution of lamellar  $\alpha$  is promoted by different magnitudes of strain gradient in different regions.

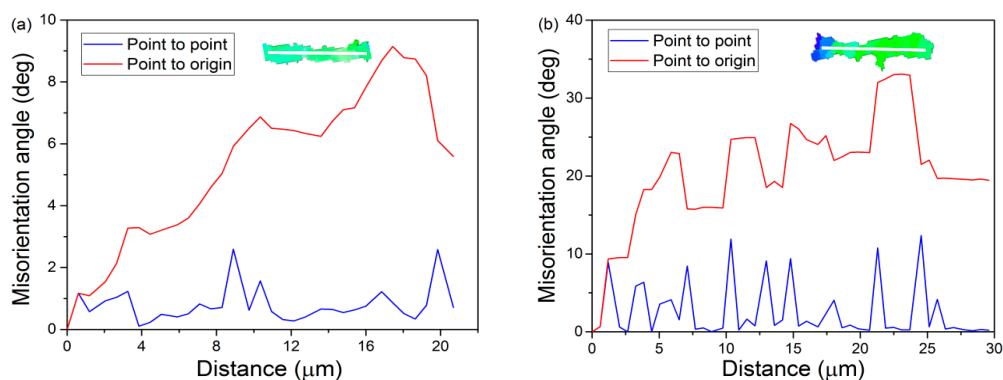


**Figure 10.** Variation in orientation along the white line marked in Figure 9: (a) L1; (b) L2.

The dynamic globularization of lamellar  $\alpha$  is generally considered to be a type of dynamic recrystallization (DRX) related to the evolution of grain boundary [29,30]. To obtain a better understanding of the deformation mechanism, it is necessary to quantitatively investigate the generation and distribution of low-angle grain boundaries (LABs) and high-angle grain boundaries (HABs). The effects of initial lamellar thickness on the distribution of grain boundary misorientation for the Ti-5.4Al-3.7Sn-3.3Zr-0.5Mo-0.4Si alloy are shown in Figure 11. For the alloy with microstructure A deformed at 960 °C, 0.01 s<sup>-1</sup>, the grain boundaries consisted of approximate 28.7% LABs and 71.3% HABs. The fraction of HABs under the same deformation conditions for microstructure B is about 44.1% (Figure 11d), while this value decreases to approximately 26.2% in microstructure C (Figure 11f). Based on the microstructures discussed above, it is considered that the volume fraction of dynamic globularization is correlated to the ratio of LABs to HABs [31]. As the grain boundary angle of the produced substructures becomes larger, DRX occurs more easily [32]. More HABs suggest a more intensive dynamic globularization process in lamellar  $\alpha$  which results in the increase in the volume fraction of globularized  $\alpha$  phase. Thus, refining the initial lamellar thickness could promote the dynamic recrystallization of  $\alpha$  phase. The effects of deformation parameters on the frequency of LABs for certain types of titanium alloys during hot deformation have been discussed in [33–35], and results showed that the grain boundary misorientation gradually increased and the ratio of LABs decreased when the alloy was deformed at a lower strain rate with a higher strain. It is generally accepted that the grain boundary evolution is coincident with continuous dynamic recrystallization (CDRX), during which the dislocation interaction induces the accumulation of LABs and formation of HABs leads to the lamellar  $\alpha$  decomposition [5,29,36]. This suggests that the microstructure evolution mechanism for the fragmentation of lamellar  $\alpha$  is dominantly predominated by the CDRX.

The EBSD maps including distribution information about grain boundaries, kernel average misorientation (KAM), and recrystallized fraction (DRX) for the alloy with initial thin lamellar microstructure are illustrated in Figure 12. The HABs mainly distributed in the equiaxed  $\alpha$  caused by dynamic globularization, whereas the LABs were always generated inside  $\alpha$  lamellae representing the features of substructures. As shown in the KAM map, the high local misorientation inside of the lamellae variants indicated the general accumulation of dislocation density and stored energy, which accelerated the forming of substructures (yellow regions in the DRX map). In particular, it can be clearly observed that a part of new fine equiaxed grains with high-angle boundaries significantly formed around the primary lamellar  $\alpha$ . At the interface of  $\alpha$  lamellae, the dislocation densities became lower and obvious recrystallized grains were observed. Therefore, these results indicate the interesting fact that a discontinuous dynamic recrystallization (DDRX) mechanism occurs and plays an important role in dynamic globularization during the deformation process for the studied alloy with initial acicular microstructure. The work by Matsumoto et al. [37] investigated the frequent occurrence of DDRX in the Ti-6Al-4V alloy and found that DDRX becomes the dominant deformation mechanism by changing the starting microstructure from the ( $\alpha + \beta$ ) to an acicular  $\alpha'$  martensite one. He et al. [38] revealed that the recrystallization mechanism changed to DDRX at a higher temperature (850 °C) in the Ti-6Al-2Zr-1Mo-1V alloy. The relative random distribution of the crystal orientations shown in Figure 9 also validates the conventional deformation feature. However, the DDRX mechanism could not be observed in the deformed microstructure during the globularization process of the alloy with initial thick lamellar microstructure.

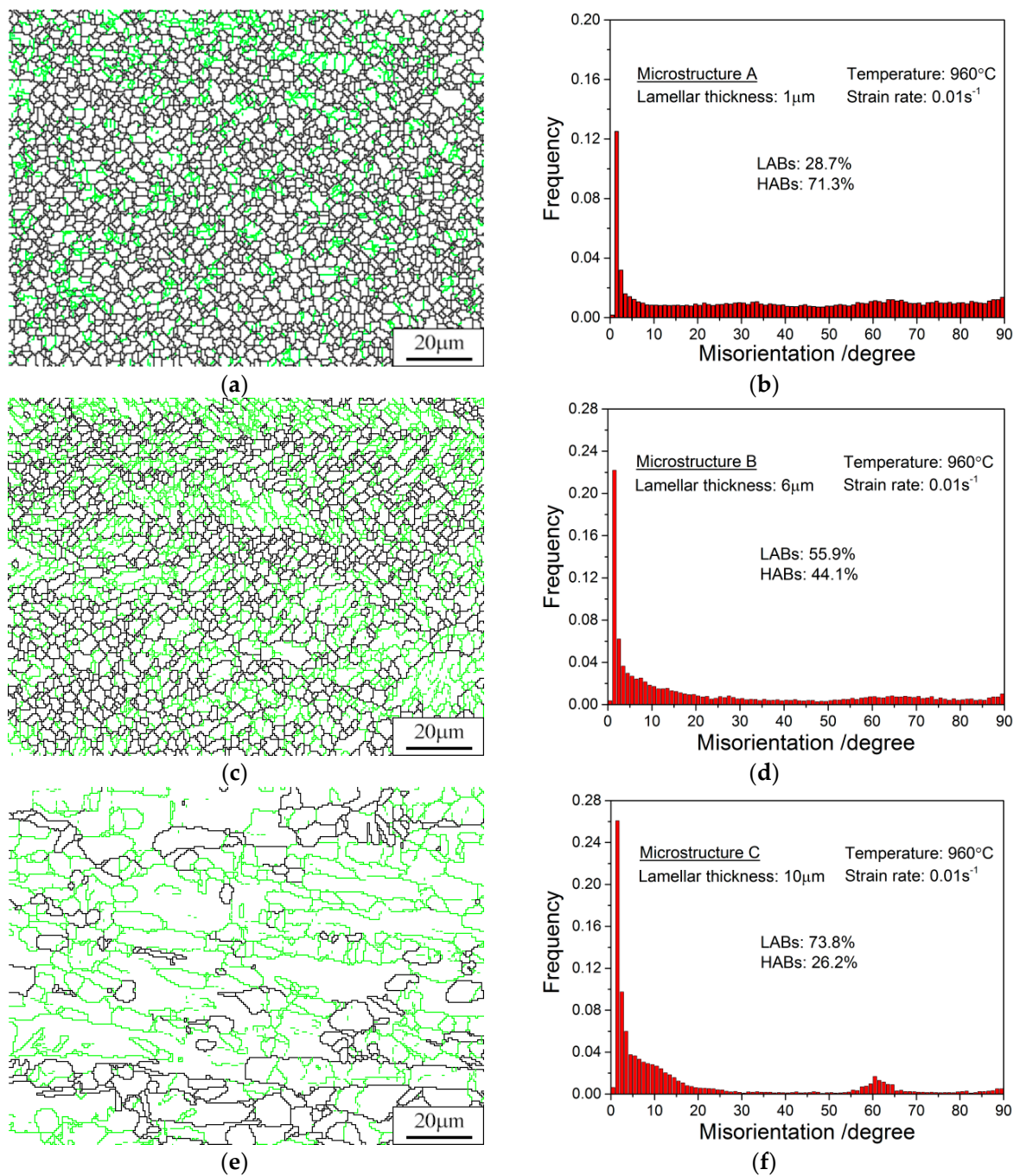


**Figure 11.** EBSD grain boundaries maps for the Ti-5.4Al-3.7Sn-3.3Zr-0.5Mo-0.4Si alloy with different initial lamellar microstructures deformed at: (a) microstructure A, 960 °C, 0.01 s<sup>-1</sup>, 0.65; (c) microstructure B, 960 °C, 0.01 s<sup>-1</sup>, 0.65; and (e) microstructure C, 960 °C, 0.01 s<sup>-1</sup>, 0.65. (b,d,f) are the corresponding misorientation distribution maps.

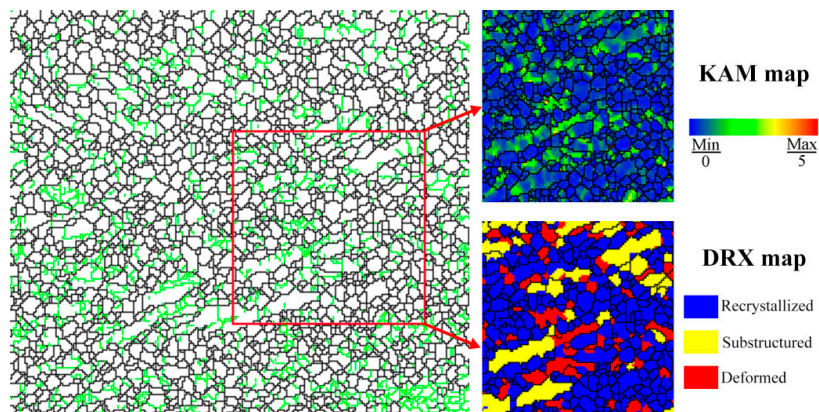


**Figure 12.** EBSD maps for the Ti-5.4Al-3.7Sn-3.3Zr-0.5Mo-0.4Si alloy with initial microstructure A (acicular-platelet) deformed at 960 °C, 0.01 s<sup>-1</sup>, region A. The green lines correspond to LABs (misorientation: 2–15°) and black lines represent HABs (misorientation >15°).

The schematic diagrams for lamellar  $\alpha$  evolution behavior for the alloy with initial thin (microstructure A: acicular-platelet) and thick (microstructure C: colony-lamellae) lamellar microstructures are illustrated in Figure 13. At the beginning of deformation, some of the thick lamellae with specific orientations may undergo severe kinking and buckling. In addition, the rest of the colonies are elongated to a certain extent and tend to twirl toward the direction perpendicular to the applied stress. With further imposed strain, the kinking of lamellar  $\alpha$  is enhanced which provides more nucleation sites and contributes to the breakdown of the lamellae. As is seen in Figure 13, the grooves were generated at the edge of  $\alpha$  lamellae promoting the fragmentation of long lamellae. Moreover, the underlying mechanism of this fragmentation process was associated with CDRX. Meanwhile, the lamellae were fully rotated and finally perpendicular to the compression direction. Then the number of globular  $\alpha$  and short  $\alpha$  laths increased with the increasing strain until the fully equiaxed microstructure was obtained. In addition, compared with the initial colony lamellar microstructure, the microstructure conversion characteristics for alloy with initial acicular microstructure were distinct owing to the various thicknesses of lamellar  $\alpha$ . During the evolution process, the phenomena of lamellar kinking were rarely observed, whereas the similar elongation and rotation behavior were visible. As pointed out in the above discussion, numerous new fine grains were formed at the interface of  $\alpha$  lamellae as a result of DDRX. Thus, in the present work, it is suggested that the collaborative mechanism of CDRX and DDRX contributes to rapid globularization of the acicular microstructure. Furthermore, the CDRX is dominant for the dynamic globularization of initial thick lamellar microstructure throughout the whole deformation process.

According to above discussions on microstructural evolution, it is concluded that the maximum value and the regions with high efficiency of power dissipation under low strain rates decrease with the increase in the initial lamellar thickness. This may be associated with a larger extent of dynamic globularization for the thin alpha lamellae as compared with the thick one. Moreover, the micrographs clearly reveal that the volume fraction of dynamic globularization increases at a higher temperature and a lower strain rate. Compared with the deformation under low strain rates of 0.01 s<sup>-1</sup> and 0.001 s<sup>-1</sup>, lamellar  $\alpha$  tends to be elongated and kinked with increasing strain rate under the temperature ranges of 900–990 °C, indicating a less sufficient dynamic globularization. On the other hand, a high efficiency of power dissipation at a moderate strain rate and temperatures ranging from 990 °C to 1020 °C is attributed to the significant  $\alpha$  to  $\beta$  phase transformation and dynamic recrystallization of  $\beta$  grains. The flow localization and local lamellar kinking may result in the occurrence of flow instability. Moreover, the present work is the first to discuss the diverse deformation mechanisms involved in the collaborative behavior of CDRX and DDRX for dynamic globularization of lamellar  $\alpha$  with different initial thicknesses on the near- $\alpha$  Ti-5.4Al-3.7Sn-3.3Zr-0.5Mo-0.4Si alloy.

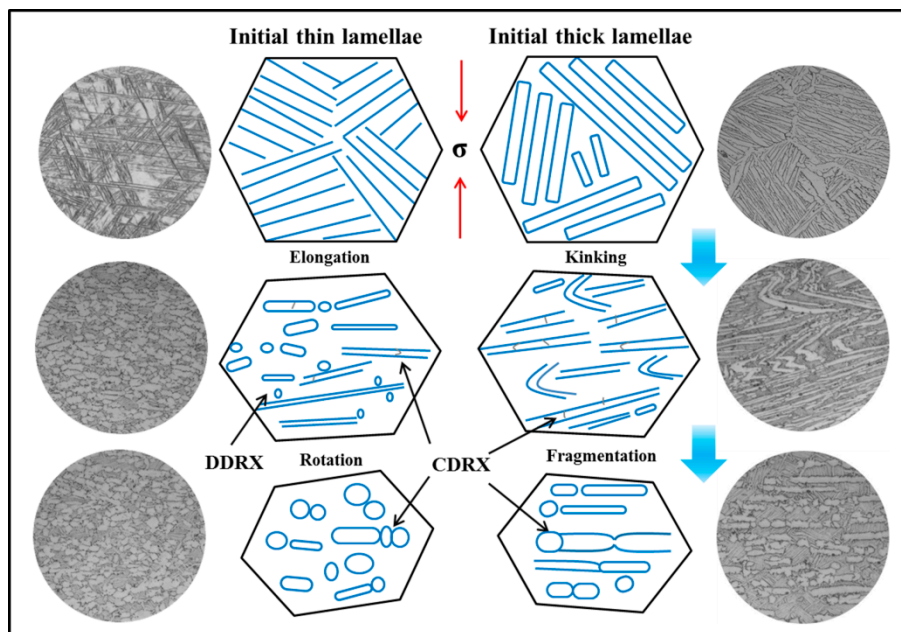


**Figure 13.** Schematic diagrams of the evolution lamellar  $\alpha$  phase with various initial thicknesses during hot deformation.

#### 4. Conclusions

In this work, the characterization of hot deformation behavior and microstructural evolution of a near- $\alpha$  Ti-5.4Al-3.7Sn-3.3Zr-0.5Mo-0.4Si alloy with various initial lamellar microstructures was investigated by a series of isothermal compression tests at a temperature range from 900 °C to 1020 °C and a strain rate range from 0.001 s<sup>-1</sup> to 10 s<sup>-1</sup>. The main conclusions are drawn as follows:

(1) The flow stress of the Ti-5.4Al-3.7Sn-3.3Zr-0.5Mo-0.4Si alloy is greatly dependent on the initial lamellar thickness and deformation parameters. The alloy with thinner initial lamellar thickness shows a higher flow stress, and an increasing deformation temperature or a decreasing strain rate can reduce the flow resistance.

(2) The peak efficiency in the processing maps occurred at a strain of 0.65 for all positioned at 960 °C/0.001 s<sup>-1</sup> with the maximum value of 0.57, 0.53, and 0.48, respectively, for the alloy with initial microstructure A, B, and C. The flow instability regions appear to expand more widely with the increase in the initial lamellar thickness when the alloy was deformed at higher strain rates.

(3) The microstructure observations indicate that different extents of globularization, elongating, kinking, and phase transformation of lamellar  $\alpha$  are responsible for the variation in power dissipation in the processing maps. The collaborative mechanism of CDRX and DDRX accelerates the globularization behavior for the thin acicular initial microstructure. For the thick initial lamellar microstructure, CDRX leading to the fragmentation of lamellae is the dominant mechanism throughout the deformation process.

**Author Contributions:** H.L. and Z.Z. conceived and designed the experiments. H.L. analyzed the data and wrote the draft preparation. Z.Z. and Y.N. reviewed the paper. H.G. and Z.Y. provided guidance and much support during the work. All authors read and approved the final manuscript.

**Funding:** This work was financially supported by the National Natural Science Foundation of China (Grant No. 51205319), the National Natural Science Foundation of Shanxi Province (No. 2015JQ5152), and the Fundamental Research Funds for the Central Universities (Grant No. 3102016ZY010).

**Conflicts of Interest:** The authors declare no conflict of interest.

## References

1. Poorganji, B.; Yamaguchi, M.; Itsumi, Y.; Matsumoto, K.; Tanaka, T.; Asa, Y.; Miyamoto, G.; Furuhashi, T. Microstructure evolution during deformation of a near- $\alpha$  titanium alloy with different initial structures in the two-phase region. *Scripta Mater.* **2009**, *61*, 419–422. [[CrossRef](#)]
2. Balasundar, I.; Raghu, T.; Kashyap, B.P. Hot working and geometric dynamic recrystallisation behaviour of a near- $\alpha$  titanium alloy with acicular microstructure. *Mater. Sci. Eng. A* **2014**, *600*, 135–144. [[CrossRef](#)]
3. Peng, W.W.; Zeng, W.D.; Wang, Q.J.; Zhao, Q.Y.; Yu, H.Q. Effect of processing parameters on hot deformation behavior and microstructural evolution during hot compression of as-cast Ti60 titanium alloy. *Mater. Sci. Eng. A* **2014**, *593*, 16–23. [[CrossRef](#)]
4. Zhao, Z.L.; Li, H.; Fu, M.W.; Guo, H.Z.; Yao, Z.K. Effect of the initial microstructure on the deformation behavior of Ti60 titanium alloy at high temperature processing. *J. Alloy. Compd.* **2014**, *617*, 525–533. [[CrossRef](#)]
5. Shams, S.A.A.; Mirdamadi, S.; Abbasi, S.M.; Kim, D.; Lee, C.S. Mechanism of martensitic to equiaxed microstructure evolution during hot deformation of a near-alpha Ti alloy. *Metall. Mater. Trans. A* **2017**, *48*, 2979–2992. [[CrossRef](#)]
6. Jackson, M.; Jones, N.G.; Dye, D.; Dashwood, R.J. Effect of initial microstructure on plastic flow behaviour during isothermal forging of Ti-10V-2Fe-3Al. *Mater. Sci. Eng. A* **2009**, *501*, 248–254. [[CrossRef](#)]
7. Lin, Y.C.; Jiang, X.Y.; Shuai, C.J.; Zhao, C.Y.; He, D.G.; Chen, M.S.; Chen, C. Effects of initial microstructures on hot tensile deformation behaviors and fracture characteristics of Ti-6Al-4V alloy. *Mater. Sci. Eng. A* **2018**, *711*, 293–302. [[CrossRef](#)]
8. Gao, P.F.; Zhan, M.; Fan, X.G.; Lei, Z.N.; Cai, Y. Hot deformation behavior and microstructure evolution of TA15 titanium alloy with nonuniform microstructure. *Mater. Sci. Eng. A* **2017**, *689*, 243–251. [[CrossRef](#)]
9. Semiatin, S.L.; Bieler, T.R. The effect of alpha platelet thickness on plastic flow during hot working of Ti-6Al-4V with a transformed microstructure. *Acta Mater.* **2001**, *49*, 3565–3573. [[CrossRef](#)]
10. Semiatin, S.L.; Seetharaman, V.; Weiss, I. Flow behavior and globularization kinetics during hot working of Ti-6Al-4V with a colony alpha microstructure. *Mater. Sci. Eng. A* **1999**, *263*, 257–271. [[CrossRef](#)]
11. Shell, E.B.; Semiatin, S.L. Effect of initial microstructure on plastic flow and dynamic globularization during hot working of Ti-6Al-4V. *Metall. Mater. Trans. A* **1999**, *30*, 3219–3229. [[CrossRef](#)]
12. Semiatin, S.L.; Bieler, T.R. Effect of texture and slip mode on the anisotropy of plastic flow and flow softening during hot working of Ti-6Al-4V. *Metall. Mater. Trans. A* **2001**, *32*, 1787–1799. [[CrossRef](#)]
13. Wanjara, P.; Jahazi, M.; Monajati, H.; Yue, S. Influence of thermomechanical processing on microstructural evolution in near- $\alpha$  alloy IMI834. *Mater. Sci. Eng. A* **2006**, *416*, 300–311. [[CrossRef](#)]
14. Peng, W.W.; Zeng, W.D.; Wang, Q.J.; Yu, H.Q. Characterization of high-temperature deformation behavior of as-cast Ti60 titanium alloy using processing map. *Mater. Sci. Eng. A* **2013**, *571*, 116–122. [[CrossRef](#)]
15. Wang, Z.; Wang, X.N.; Zhu, Z.S. Characterization of high-temperature deformation behavior and processing map of TB17 titanium alloy. *J. Alloy. Compd.* **2017**, *692*, 149–154. [[CrossRef](#)]
16. Sun, Y.; Feng, X.Y.; Hu, L.X.; Zhang, H.; Zhang, H.Z. Characterization on hot deformation behavior of Ti-22Al-25Nb alloy using a combination of 3D processing maps and finite element simulation method. *J. Alloy. Compd.* **2018**, *753*, 256–271. [[CrossRef](#)]
17. Li, H.; Zhao, Z.L.; Guo, H.Z.; Yao, Z.K.; Ning, Y.Q.; Miao, X.P.; Ge, M.M. Effect of initial alpha lamellar thickness on deformation behavior of a near- $\alpha$  high-temperature alloy during thermomechanical processing. *Mater. Sci. Eng. A* **2017**, *682*, 345–353. [[CrossRef](#)]
18. Prasad, Y.V.R.K.; Gegel, H.L.; Doraivelu, S.M.; Malas, J.C.; Morgan, J.T.; Lark, K.A.; Barker, D.R. Modeling of dynamic material behavior in hot deformation: forging of Ti-6242. *Metal. Trans. A* **1984**, *15*, 1883–1892. [[CrossRef](#)]
19. Lin, Y.C.; Li, L.; Xia, Y.; Jiang, Y. Hot deformation and processing map of a typical Al-Zn-Mg-Cu alloy. *J. Alloy. Compd.* **2013**, *550*, 438–445. [[CrossRef](#)]
20. Saxena, K.K.; Pancholi, V.; Jha, S.K.; Chaudhari, G.P.; Srivastava, D.; Dey, G.K. A novel approach to understand the deformation behavior in two phase region using processing map. *J. Alloy. Compd.* **2017**, *706*, 511–519. [[CrossRef](#)]
21. Prasad, Y.V.R.K.; Seshacharyulu, T.; Medeiros, S.C.; Frazier, W.G. Influence of oxygen content on the forging response of equiaxed ( $\alpha + \beta$ ) preform of Ti-6Al-4V: commercial vs. ELI grade. *J. Mater. Process. Tech.* **2001**, *108*, 320–327. [[CrossRef](#)]

22. Semiatin, S.L.; Seetharaman, V.; Weiss, I. Hot workability of titanium and titanium aluminide alloys—An overview. *Mater. Sci. Eng. A* **1998**, *243*, 1–24. [[CrossRef](#)]
23. Li, A.B.; Huang, L.J.; Meng, Q.Y.; Geng, L.; Cui, X.P. Hot working of Ti-6Al-3Mo-2Zr-0.3Si alloy with lamellar  $\alpha + \beta$  starting structure using processing map. *Mater. Des.* **2009**, *30*, 1625–1631. [[CrossRef](#)]
24. Li, X.; Lu, S.Q.; Fu, M.W.; Wang, K.L.; Dong, X.J. The optimal determination of forging process parameters for Ti-6.5Al-3.5Mo-1.5Zr-0.3Si alloy with thick lamellar microstructure in two phase field based on P-map. *J. Mater. Process. Tech.* **2010**, *210*, 370–377. [[CrossRef](#)]
25. Kumar, B.K.; Saxena, K.K.; Dey, S.R.; Pancholi, V.; Bhattacharjee, A. Processing map-microstructure evolution correlation of hot compressed near alpha titanium alloy (TiHy 600). *J. Alloy. Compd.* **2017**, *691*, 906–913.
26. Wan, Z.P.; Hu, L.X.; Sun, Y.; Wang, T.; Li, Z. Hot deformation behavior and processing workability of a Ni-based alloy. *J. Alloy. Compd.* **2018**, *769*, 367–375. [[CrossRef](#)]
27. Zhao, Z.B.; Wang, Q.J.; Liu, J.R.; Yang, R. Characterizations of microstructure and crystallographic orientation in a near- $\alpha$  titanium alloy billet. *J. Alloy. Compd.* **2017**, *712*, 179–184. [[CrossRef](#)]
28. Delannay, L.; Mishin, O.V.; Jensen, D.J.; Van Houtte, P. Quantitative analysis of grain subdivision in cold rolled aluminium. *Acta Mater.* **2001**, *49*, 2441–2451. [[CrossRef](#)]
29. Balasundar, I.; Raghu, T.; Kashyap, B.P. Processing map for a cast and homogenized near alpha titanium alloy. *Int J. Mater. Form.* **2015**, *8*, 85–97. [[CrossRef](#)]
30. Seshacharyulu, T.; Medeiros, S.C.; Frazier, W.G.; Prasad, Y. Microstructural mechanisms during hot working of commercial grade Ti-6Al-4V with lamellar starting structure. *Mater. Sci. Eng. A* **2002**, *325*, 112–125. [[CrossRef](#)]
31. Jia, J.B.; Zhang, K.F.; Lu, Z. Dynamic globularization kinetics of a powder metallurgy Ti-22Al-25Nb alloy with initial lamellar microstructure during hot compression. *J. Alloy. Compd.* **2014**, *617*, 429–436. [[CrossRef](#)]
32. Niu, H.Z.; Kong, F.T.; Chen, Y.Y.; Yang, F. Microstructure characterization and tensile properties of  $\beta$  phase containing TiAl pancake. *J. Alloy. Compd.* **2011**, *509*, 10179–10184. [[CrossRef](#)]
33. Wang, K.; Wu, M.Y.; Yan, Z.B.; Li, D.R.; Xin, R.L.; Liu, Q. Dynamic restoration and deformation heterogeneity during hot deformation of a duplex-structure TC21 titanium alloy. *Mater. Sci. Eng. A* **2018**, *712*, 440–452. [[CrossRef](#)]
34. Fan, X.G.; Zheng, H.J.; Zhang, Y.; Zhang, Z.Q.; Gao, P.F.; Zhan, M.; Liu, J. Acceleration of globularization during interrupted compression of a two-phase titanium alloy. *Mater. Sci. Eng. A* **2018**, *720*, 214–224. [[CrossRef](#)]
35. Sun, J.Z.; Li, M.Q.; Li, H. Deformation behavior of TC17 titanium alloy with basketweave microstructure during isothermal compression. *J. Alloy. Compd.* **2018**, *730*, 533–543. [[CrossRef](#)]
36. Li, L.; Luo, J.; Yan, J.J.; Li, M.Q. Dynamic globularization and restoration mechanism of Ti-5Al-2Sn-2Zr-4Mo-4Cr alloy during isothermal compression. *J. Alloy. Compd.* **2015**, *622*, 174–183. [[CrossRef](#)]
37. Matsumoto, H.; Bin, L.; Lee, S.; Li, Y.; Ono, Y.; Chiba, A. Frequent Occurrence of Discontinuous Dynamic Recrystallization in Ti-6Al-4V Alloy with  $\alpha'$  Martensite Starting Microstructure. *Metall. Mater. Trans. A* **2013**, *44*, 3245–3260. [[CrossRef](#)]
38. He, D.; Zhu, J.C.; Lai, Z.H.; Liu, Y.; Yang, X.W. An experimental study of deformation mechanism and microstructure evolution during hot deformation of Ti-6Al-2Zr-1Mo-1V alloy. *Mater. Des.* **2013**, *46*, 38–48. [[CrossRef](#)]

